Structure-driven tuning of O and CO adsorption on AuCu nanoparticles: A density functional theory study

Ilya V. Chepkasov [ORCID],[*] Viktor S. Baidyshev [ORCID], and Alexander G. Kvashnin [ORCID]
Skolkovo Institute of Science and Technology, Moscow 121205, Russian Federation

Nanoparticles are fascinating nanoobjects that are actively studied and widely employed in various fields, such as heterogeneous catalysis and advanced electrode materials. Their local atomic structure and composition can significantly impact their properties. We employed the state-of-the-art first-principles calculations to investigate the effects of AuCu nanoparticle structure and composition on the electronic properties, charge distribution, and CO and O adsorption energies. Two types of nanoparticles were examined in this study; specifically core-shell nanoparticles (Cu@Au, Au@Cu) and bimetallic alloy particles (Au-Cu), all with an average diameter of 2 nm (321 atoms) and exhibiting fcc, icosahedral, and amorphous structures. The research comprehensively investigated the electronic and adsorption properties of the proposed nanoparticles with regard to their ability to adsorb CO and O, revealing the potential for finely tuning of their properties by modifying their atomic structure and composition. Adjusting the core-to-shell ratio allows one to precisely tune the O and CO adsorption energies on the nanoparticle surface, particularly in fcc nanoparticles. This results in a narrower range of adsorption energies, specifically for CO adsorption, which cannot be achieved in bimetallic alloys. Our study shows the significance of this approach for fine-tuning adsorption energies on a nanoparticle surface.

I. INTRODUCTION

Metal nanoparticles are widely used in heterogeneous catalysis due to their high surface area to the volume ratio, which reduces the cost of producing catalytically active elements [1–7]. Copper nanoparticles (NPs) have demonstrated suitability for CO_2 hydrogenation, regeneration reactions, and CO oxidation [8,9]. However, copper is prone to oxidation, which leads to surface poisoning, reducing their catalytic activity [10]. One successful strategy for preventing this involves alloying copper with a stabilizing metal like gold, which is resistant to corrosion and oxidation. Copper-gold bimetallic alloys are recognized as materials that are more catalytically efficient compared to their single-component counterparts [11–18]. It is therefore possible to tune the catalytic properties of bimetallic nanoparticles effectively by varying the proportions of Cu and Au. The catalytic activity of nanoparticles is primarily determined by their surface properties and strongly depends on their structural features [19,20]. In addition to bimetallic alloy, nanoparticles are capable to form core-shell structures that give them uniquely advantageous properties [21–28].

The effect of the ligand, the redistribution of the charge at the core-shell interface, and the appearance of a dimensional quantum effect in the case of a thin shell lead to a change in the catalytic properties of core-shell nanoparticles [29,30]. Another important factor is the deformation of the metallic shell due to the mismatch of its lattice with the core at the interface, which can lead to a change in the electronic proper-

ties [31]. Recent work by Zhang *et al.* [32] using the example of Au@Pd core-shell catalysts has shown that the selection of the necessary size of the core and shell can significantly increase the catalytic activity of nanoparticles.

For this reason, in our work we have studied three different models of bimetallic AuCu nanoparticles, namely Cu-core/Au-shell (Cu@Au), Au-core/Cu-shell (Au@Cu), and homogeneous bimetallic alloy particles (Cu-Au) with random distribution of Au and Cu atoms in the cluster. In order to obtain the most efficient catalyst, it is necessary to determine the atomic structure and composition of the particles.

To assess the catalytic efficiency of nanoparticles without direct calculations of the adsorption of atomic and molecular agents on the surface, there are a number of models that provide information on the reactivity of nanoparticles [33,34]. The most successful model was proposed by Hammer and Nørskov [33]. Their model, called the *d*-band model, justifies the reactivity of transition metals on the basis of a single parameter, the center of the *d*-band of the surface atoms. This model well describes the difference in adsorption energy of atoms and molecules at different sites on the surface of nanoparticle [35]. In addition to the electronic structure, the study of the surface charge can also provide important information about the chemical reactivity of nanoparticles, since the adsorption of molecules causes a charge flow that affects the bond strength [34].

Here we have studied the features of the electronic and catalytic properties of AuCu nanoparticles caused by the variation of their local atomic environment [fcc, icosahedral (Ih), and amorphous] and type (core-shell or alloy) together with the Cu:Au ratio. The prospects for the application of

_____
[*]I.Chepkasov@skoltech.ru

these nanoparticles towards CO oxidation reaction were analyzed based on the calculations of surface charges and d-band center. For nanoparticles with fcc structure, the adsorption energies of CO molecules and O atoms on the Au-Cu nanoparticles with different compositions were estimated.

II. SIMULATION METHODOLOGY

To analyze the electronic structure and reactivity of the nanoparticles using density functional theory (DFT) [36,37], we first relaxed the geometry of each studied nanoparticle. The generalized gradient approximation (GGA) was used with the revised PBE [38] parametrization for the exchange correlation functional as implemented in the VASP package [39–41]. The ion-electron interaction was described by the augmented plane wave (PAW) method [42], with a cut-off energy of 480 eV. The orbital occupancies were smeared by the first-order Methfessel-Paxton method with a smearing width of 0.05 eV.

Spin-polarized GGA with the PBE parametrization was used to calculate adsorption energies. The energy of the oxygen molecule was calculated for the triplet state using spin-polarized calculations. Effective interaction between the valence electrons and nuclei screened by frozen core electrons was described via scalar relativistic ultrasoft pseudopotentials. The integration of spin-orbit coupling with scalar relativistic pseudopotentials through the implementation of the VASP code resulted in fully relativistic results. This outcome holds significance for nanoparticles that are composed of gold.

Density functional theory is a widely used tool for studying adsorption of atoms and small molecules on metallic surfaces and nanoparticles. While generally accurate, DFT relies on the approximation of electron-electron interactions using exchange-correlation functionals. Unfortunately, these functionals often prove inadequate for describing the dispersion component of the van der Waals energies, which result from electrons responding to instantaneous charge density fluctuations. Methods for calculating the van der Waals interaction are classified into three categories: semiempirical models developed by Grimme *et al.* [43–45], models that are based on atomic polarization and are modified by the electron density [46–49], and full density functional approximations which are founded on pairwise dispersion models utilizing only the density [50,51]. As previously demonstrated [52], a comparison of three methods that include DFT-D3, DFT-D2, and optPBE dispersion corrections has shown that DFT-D2 and optPBE can yield diverse outcomes for CO adsorption on metallic nanoparticles in comparison to experimental results. Only the DFT-D3 correction yields results in accordance with experiment. In our research comparing these methods, alternative functionals have also been employed to compute the adsorption energy of the CO molecule on the surface of Au nanoparticles (see Table I). Our findings indicate that the outcomes from DFT-D3 exhibit remarkable similarity to those of the extensively employed and highly precise DFT-TS approach for describing dispersive van der Waals interactions. Consequently, we applied Grimme correction DFT-D3 [44] to account for dispersive van der Waals interaction.

The local geometry optimization of considered clusters was conducted until the maximum force on each atom became

TABLE I. Calculation methods used; E_a, energy of CO adsorption on an Au (fcc, 321 atoms) nanoparticle, and Δq, the change in charge of the CO molecule between states before and after adsorption (within the Bader theory calculation).

Method	E_a (eV)	Δq (e)
DFT-D2 [43]	−0.7837	0.160
DFT-D3 [44]	−0.6338	0.150
DFT-D3-BJ [45]	−0.6394	0.145
DFT-TS [47]	−0.6206	0.145
DFT-TS/HI [53]	−0.6201	0.155
optB86b-vdW [54]	−0.5984	0.141
optB88-vdW [54]	−0.4540	0.125
optPBE-vdW [54]	−0.3555	0.132
rev-vdW-DF2 [55]	−0.5562	0.147
SCAN-rVV10 [56]	−0.7139	0.147

less than 0.03 eV/Å. The nanoparticles were placed in a box with a vacuum of at least 10 Å separating them.

The results of the calculations were postprocessed and visualized using the Open Visualization Tool [57] and the VESTA package [58,59]. Electron transfer was explored by Bader analysis [60]. To determine the structural stability, the excess energy [61] of nanoparticles with respect to a bulk was calculated,

$$\Delta = (E_{NPs} - E_{Cu}N_{Cu} - E_{Au}N_{Au})/(N_{Cu} + N_{Au})^{2/3}, \quad (1)$$

where E_{NPs} is the energy of the considered nanoparticle; N_{Cu} and N_{Au} correspond to the number of Cu and Au atoms, respectively; E_{Cu} and E_{Au} are the energies per atom for the bulk Cu and Au, respectively.

Adsorption energies of CO molecules and O atoms were calculated as

$$E_{ads}[CO] = E[CO/Cu_xAu_y] - E[CO] - E[Cu_xAu_y], \quad (2)$$

$$E_{ads}[O] = E[O/Cu_xAu_y] - E[O_2]/2 - E[Cu_xAu_y], \quad (3)$$

where $E[CO/Cu_xAu_y]$ and $E[O/Cu_xAu_y]$ are the energies of adsorption complexes of CO and O on Cu_xAu_y nanoparticles, while $E[CO]$, $E[O_2]$, and $E[Cu_xAu_y]$ are the energies of the gas phase CO and O_2 molecules and the considered Cu_xAu_y nanoparticles, respectively.

III. RESULTS AND DISCUSSION

Our study is based on the analysis of the catalytic properties of AuCu NPs and the identification of the peculiarities of the influence of structure type, local atomic environment, and composition on their properties. We considered core-shell and bimetallic alloy AuCu NPs with a diameter of 2 nm (321 atoms) with fcc, icosahedral, and amorphous structures, so a total of nine types of NPs were considered. The atomic structures of the considered nanoparticles are shown in Fig. 1. For the Cu@Au and Au@Cu core-shell structures, we considered only compositions where the entire surface consists of Au or Cu atoms, respectively, while for NPs with a random arrangement of elements (Au-Cu), the entire range of compositions was considered. We studied different structures of AuCu NPs (fcc, icosahedral, and amorphous) because particles with both
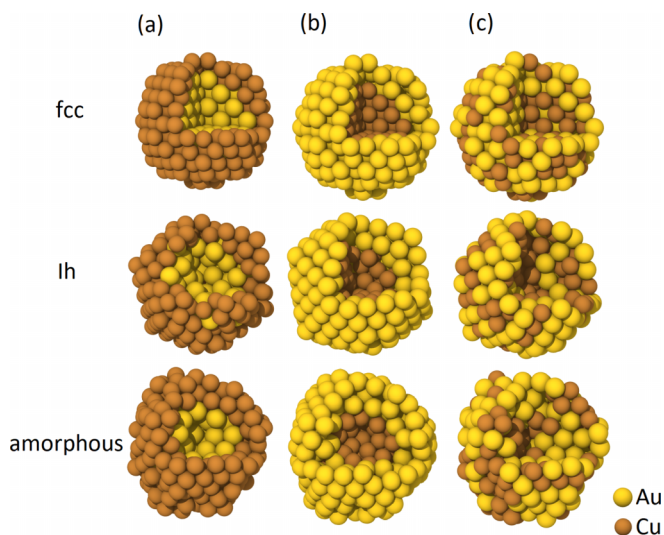
FIG. 1. Atomic structures of considered bimetallic NPs with different local environments. NPs with (a) Au core with Cu shell (Au@Cu), (b) Cu core with Au shell (Cu@Au), and (c) bimetallic alloy (Au-Cu) are shown with fcc, Ih, and amorphous structures. The gold and copper atoms are depicted as yellow and brown spheres, respectively.

fcc and icosahedral structures have been experimentally synthesized [62,63], and the use of these NPs in high-temperature catalytic reactions can lead to changes in their atomic neighborhood due to melting and/or amorphization [64–67], which should be taken into account when studying the properties of these NPs. Amorphous nanoparticles were obtained by MD modeling the fcc melting of AuCu nanoparticles and rapid freezing of the amorphous structure.

Before studying the electronic properties, surface charge and adsorption energies of CO molecules and O atoms on the Au-Cu NPs with different compositions, we estimated the energies of particles with different structures, namely fcc, icosahedral, amorphous. The excess energies (Δ) were calculated as the difference between the binding energy of the NPs and the bulk counterparts Eq. (1).

The dependence of Δ on the Au concentration in Au-Cu, Cu@Au, and Au@Cu NPs with different structures (fcc, Ih, and amorphous) are shown in Fig. 2. Comparing two types of core-shell NPs, the difference in binding energies between Cu@Au and Au@Cu NPs can be clearly seen. Au@Cu NPs are energetically less favorable compared to other structures, see Fig. 2. As can be seen, bimetallic Au-Cu NPs show an energy minimum in contrast to core-shell NPs. For fcc and icosahedral NPs [Fig. 2(a)] the energy minimum corresponds to Cu:Au = 1:1, while for amorphous particles the minimum corresponds to 90% gold in the composition. Experimental values of the "average" surface energy of Cu and Au are 1.83 J/m^2 [68] and 1.5 J/m^2 [69], respectively, indicating that the gold surface of NPs is more preferred than the copper surface. Similar results were previously observed for Au@Cu NPs [70,71], which supports our finding. In addition, our previous work [72] on the thermodynamic stability of AuCu NPs with different structural patterns using EAM potential [73] defines that the surface covered by gold possesses thermodynamic stability compared to other structure types. Moreover, the study of NPs at different temperatures showed that AuCu NPs of all four patterns (bimetallic alloy, core-shell, "Janus" type) maintain a relatively stable structure up to temperature of 700 K, while higher temperatures lead to active diffusion processes involving both copper and gold atoms, resulting in the formation of the copper-gold alloy with mixed surface composition [72].

One of the main driving forces leading to the adsorption of various chemical agents on the surface is the nonzero surface charge resulting from dangling bonds on the surface. We have studied the distribution of the surface charges for the considered NPs by using Bader's theory [60] as shown in Fig. 3. It can be seen that uniform Au-Cu alloys (fcc, Ih, and amorphous) always have an excess of electrons with an average surface charge of about $-0.025e^-$ per surface atom, see blue lines in Fig. 3. Our results show that the atomic-thick Au shell of the Cu core (green lines in Fig. 3), corresponding to the composition of $Cu_{0.5}@Au_{0.5}$, has an average surface charge four times larger compared to a pure metallic NP of the same size ($-0.1e^-$ and $-0.025e^-$ per surface atoms, respectively). This is in agreement with previous results obtained for
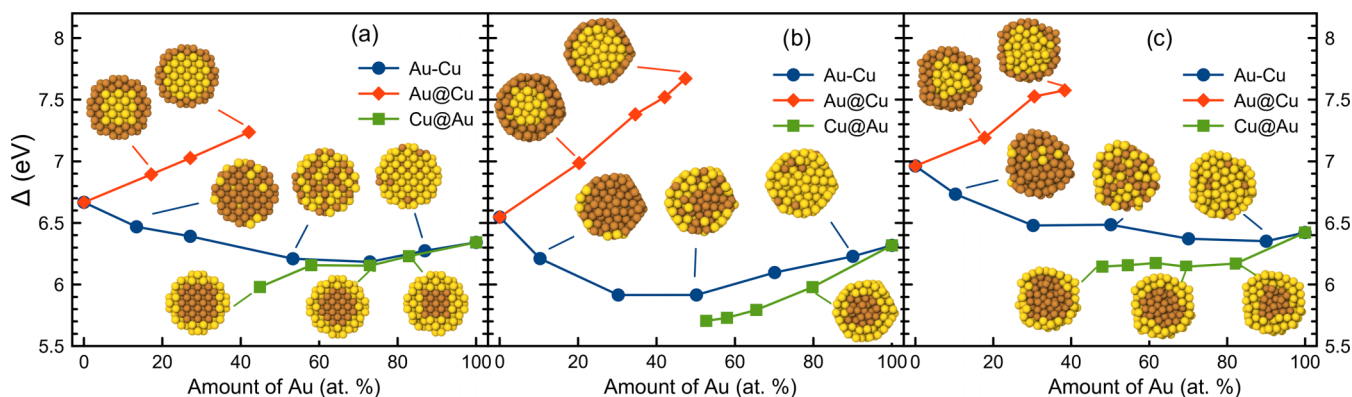

FIG. 2. Excess energies of AuCu NPs with different structure types (fcc, Ih, and amorphous) and atomic environment (Cu@Au, Au@Cu, and Au-Cu) as a function of composition. (a) fcc, (b) Ih, and (c) amorphous. The gold and copper atoms are depicted as yellow and brown spheres, respectively.
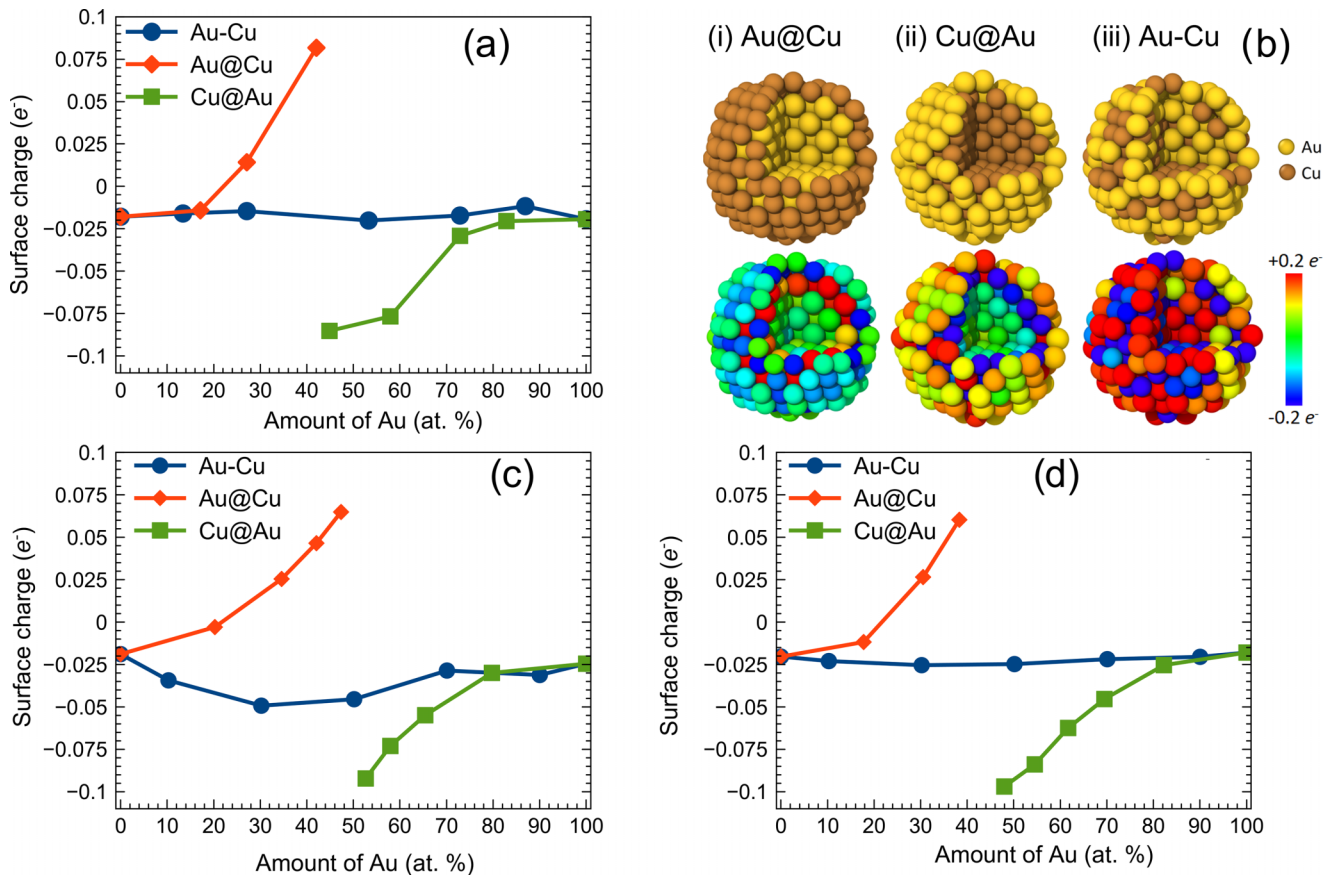
FIG. 3. Average surface charge of AuCu NPs with different structures. (a) fcc, (c) Ih, and (d) amorphous and atomic environment (Cu@Au, Au@Cu, and Au-Cu) as a function of composition. (b) Atomic structures of fcc nanoparticles with atomic charge distributions. The gold and copper atoms are depicted as yellow and brown spheres, respectively. Positive values indicate a shortage of electrons (electrons have migrated from the surface to the interior), and negative values indicate an excess of electrons resulting in a negative surface charge.

core-shell Pd@Pt NPs [74], where their surface charge is also larger compared to pure metallic ones.

The atomic thick Cu shell of the Au core shows the surface charge of $\sim -0.025e^-$ to $0.075e^-$ per surface atom (see red lines in Fig. 3) depending on the Cu:Au composition. The surface charge for Au NPs with both fcc and Ih structure types is larger compared to pure Cu NPs, namely $-0.0193e^-$ with respect to $-0.0179e^-$ for fcc and $-0.0272e^-$ with respect to $-0.0191e^-$ for Ih, see Fig. 3. This result is in good agreement with the difference in the work functions for these atom types [75].

However, in the case of the amorphous structure of NPs, the situation is reversed, namely for pure Au the charge is $-0.0196e^-$, while for Cu NP the charge is $-0.0205e^-$. We suggest that such an effect is probably observed due to the highly deformed surface of amorphous NPs. The charge difference also shows the tendency of the electron density to be redistributed from the copper atoms to the gold atoms. As a result, we can conclude that changing the ratio of atoms in the core and shell of the particle together with the type of metal on the surface (Au or Cu) drastically affects the surface charge as follows:

(1) Cu core covered by an atomic-thick Au shell shows a significant excess of electrons flowing from copper atoms to surface gold atoms, forming a negative charge on the NP surface;

(2) Au core covered by atomic-thick Cu shell shows opposite results, namely a deficiency of electrons on the surface forming a positive charge.

Thus, changing the structure of AuCu nanoparticles leads to fine-tuning of the surface charge and opens up more prospects for their use in various applications.

As mentioned above one of the successful descriptors allowing the determination of catalytic properties is the d-band center. We calculated the d-band center for all considered NPs by calculating of electronic densities of states projected onto each atom in the NP. The only surface atoms were selected for analysis and the d-band center values of the surface were averaged. The results are shown in Fig. 4. Calculations showed that average surface d-band center for Au are -3.22, -3.28, and $-3.32\,\text{eV}$ for fcc, icosahedral, and amorphous structure types (Fig. 4). For Cu surfaces where the average d-band centers were -2.32, -2.41, and $-2.35\,\text{eV}$ for fcc, icosahedral, and amorphous structure types. Considering this, it can be concluded that the structure type of the NP slightly influences the d-band center, see Fig. 4.

Core-shell structures, in which the Cu or Au core is covered by an atomic-thick shell (Au or Cu atoms, respectively), show the maximum or minimum values of the d-band center among all other NPs. For Au@Cu NPs, the maximum values for Au:Cu = 1:1 are close to -2.11, -2.14, and $-2.16\,\text{eV}$ for fcc, icosahedral, and amorphous structures, respectively,
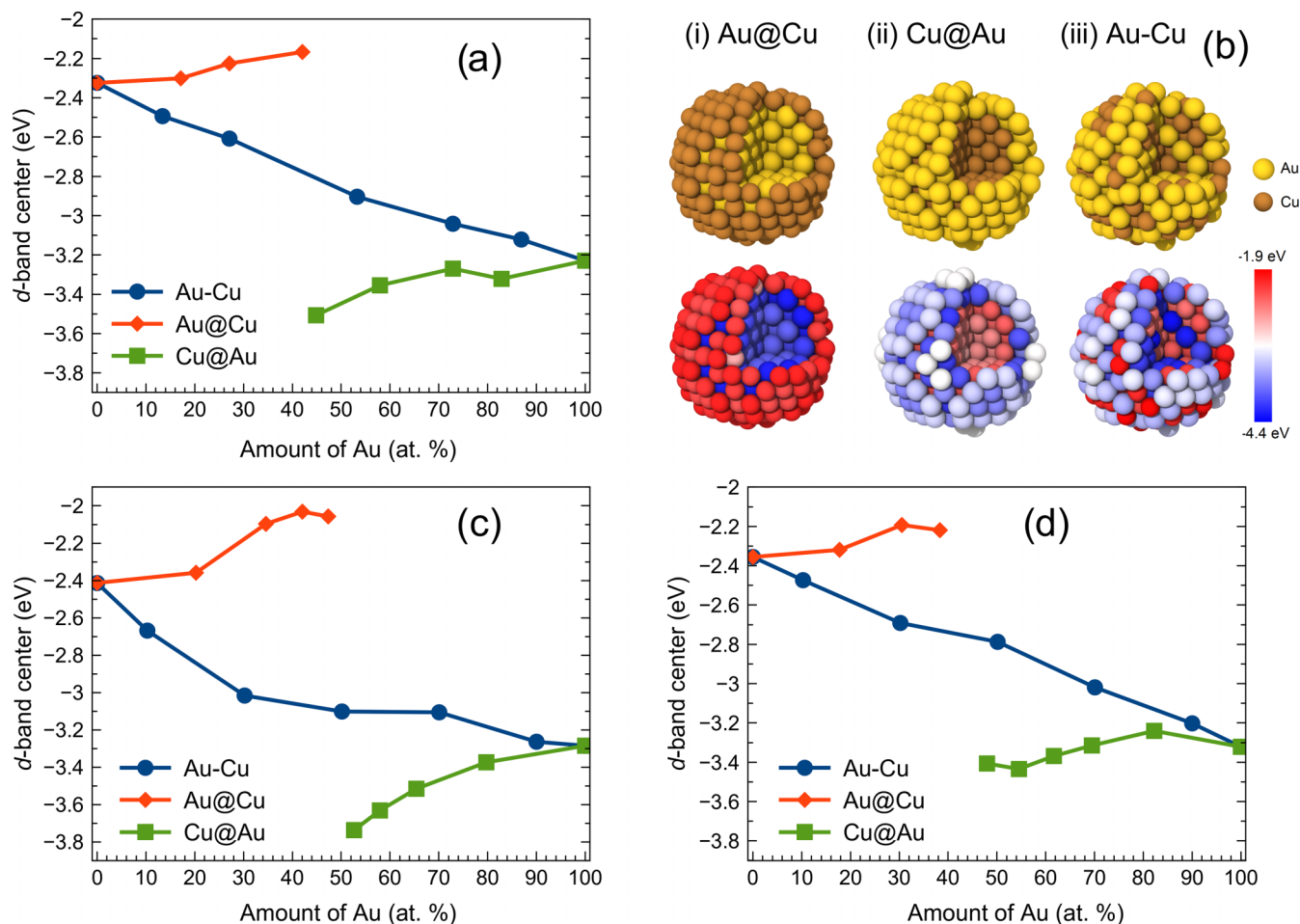
FIG. 4. d-band centers averaged over the surface of AuCu nanoparticles with (a) fcc, (c) Ih, and (d) amorphous structure types and atomic environment (Cu@Au, Au@Cu, and Au-Cu) as a function of composition. (b) Atomic structures of fcc nanoparticles with spatial distribution of d-band center values. The gold and copper atoms are depicted as yellow and brown spheres, respectively.

while Cu@Au NPs showed minimum values of d-band center of -3.55, -3.77, and -3.42 eV for fcc, icosahedral, and amorphous structure, respectively. In contrast to the core-shell NPs, the alloy particles show an almost monotonic decrease of the d-band center dependence with respect to Au concentration (blue lines in Fig. 4).

In the case of icosahedral Cu@Au [green line in Fig. 4(c)] we observed the smallest value of the d-band center of -3.77 eV among all other NPs corresponding to the core-shell Cu@Au NP with almost 50% of gold in the composition. As shown in Ref. [76], the lower the value of the d-band center, the weaker the binding energy of the adsorbents with the metal surface. However, according to the Sabatier principle, the adsorption energy should be neither too strong nor too weak for the adsorbent to interact with the catalyst surface. Thus, changing the ratio of core and shell atoms in the AuCu NP can lead to significant changes in the surface properties of NPs, i.e., the d-band center.

To visualize the charge transfer between Au and Cu atoms in Cu@Au and Au@Cu nanoparticles, we analyzed the difference between the electron density of the core and shell (Fig. 5). Our findings show that in Au@Cu nanoparticles, the electron density localisation shifts from the copper atoms to the region near the subsurface gold atoms, resulting in a

shortage of electrons at the nanoparticle surface [Fig. 5(b)]. In the case of Cu@Au, there is a shift of electron density from subsurface copper atoms to surface gold atoms, resulting in electron excess formation at the nanoparticle's surface [Fig. 5(a)].
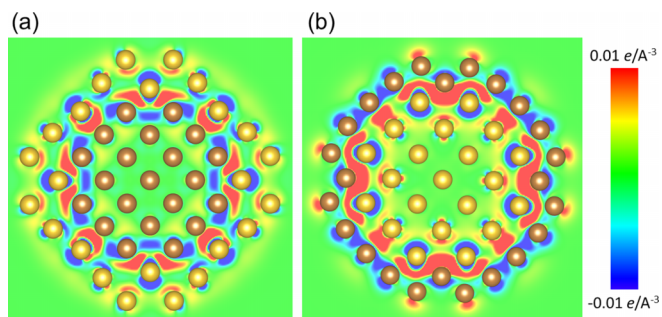

FIG. 5. Charge transfer between Au and Cu atoms in Cu@Au and Au@Cu nanoparticles visualized as a difference between the electron density of core and shell. Red areas correspond to density build-up and blue to depletion. (For interpretation of the references to color in this figure legend, the reader is referred to the web version of this article). The gold and copper atoms are depicted as yellow and brown spheres, respectively.
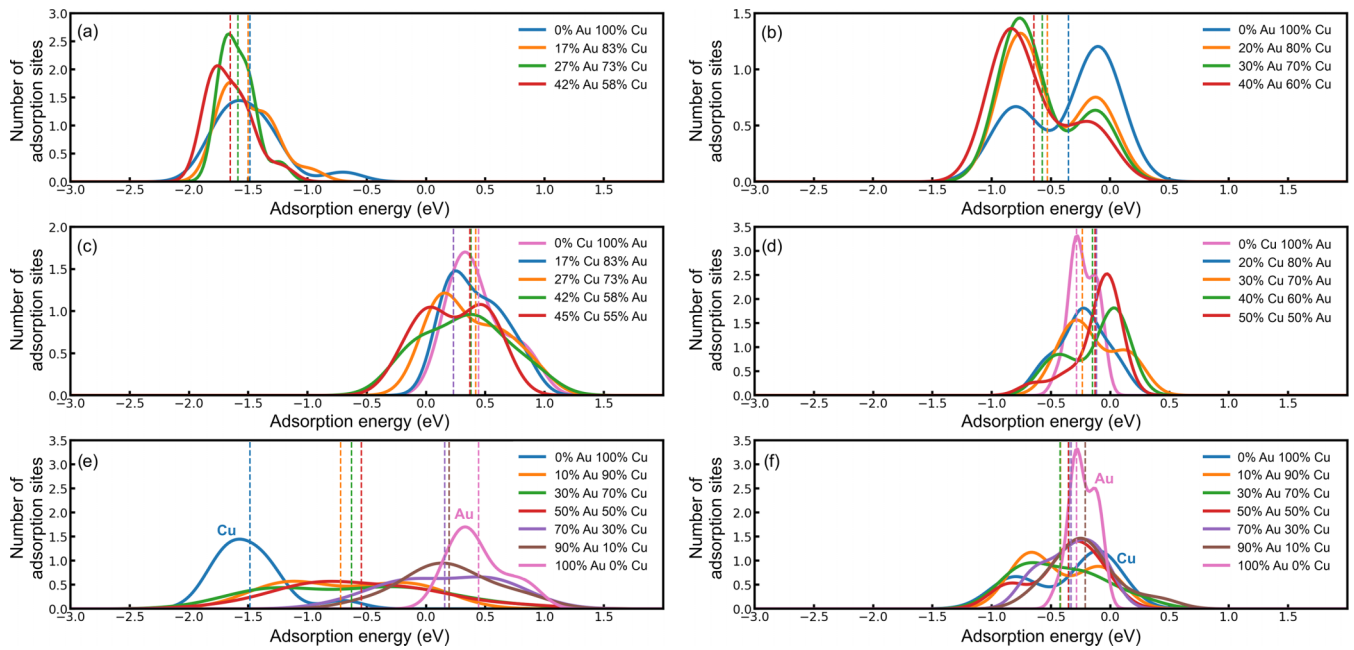
FIG. 6. Distributions of adsorption energies of O and CO species calculated for 14 symmetrical nonequivalent adsorption sites on fcc core-shell nanoparticles (Cu@Au and Au@Cu). The distributions were obtained by applying 0.35 eV smearing to the calculated adsorption energies. The dashed lines reflect the average adsorption energies calculated for each distribution.

The next part of the study is devoted to the investigation of the adsorption of O and CO on the NPs. Since the dependence on the structure type was previously studied in Ref. [77], we paid more attention to the influence of the adsorption properties on the composition of the NPs. We chose the fcc structure type as a model system for this study, which allows us to show the general tendencies in the adsorption of O and CO on the AuCu NPs. In order to determine the influence of the local atomic environment of AuCu NPs on the adsorption energy of O and CO, we considered 14 different adsorption sites on the surface of AuCu nanoparticles with fcc structure. In order for the adsorption pattern to be most complete, a variety of adsorption sites were chosen including top, bridge, hollow, and kink (see Supplemental Material [79]).

The selected 14 adsorption sites were fixed for all the studied nanoparticles (core-shell and bimetallic) in order to distinguish how the local atomic environment influences the adsorption. During the calculation of the adsorption energy, the positions of the atoms in the particle were frozen and only the adsorbent was allowed to move. As shown by Ma *et al.* [78] calculating the adsorption energy with frozen atoms of a nanoparticle can lead to overestimated values of the adsorption energy. We have carried out comparative calculations of the adsorption energy of CO on Cu@Au nanoparticles. We calculated the adsorption of CO at 14 sites on a frozen nanoparticle and a completely free (nonfrozen atoms) nanoparticle. The results of the calculations are presented in the supplemental material [79]. The calculation results show that when the particle is frozen, the adsorption energy is slightly higher than when the particle is unfrozen, although the site-dependent adsorption energy trends are fully conserved (except for site 11 where frozen nanoparticle optimization shifted the molecule to another more advantageous site).

The adsorption energies of O and CO on the copper-terminated surface of Au@Cu nanoparticles are lower than those for Cu@Au nanoparticles with Au surface (Fig. 6). Similar observation was also found in our previous work [77] where small AuCu nanoparticles were studied. The adsorption energy of oxygen on Au@Cu nanoparticles [Fig. 6(a)] is almost independent of the concentration of Au with respect to Cu and the average values are around −1.5 eV. A more interesting situation is observed for the adsorption of CO on Au@Cu NPs [Fig. 6(b)], where the average adsorption energy of CO on the pure gold NP is around −0.4 eV, showing the highest values compared to other compositions; adsorption energies for other compositions of Au@Cu NPs are around −0.55 eV, Fig. 6(b). For Cu@Au nanoparticles the average values of adsorption energies of both CO and O are higher compared to the previously considered Au@Cu NPs [Figs. 6(c) and 6(d)]. The average adsorption energy of O [Fig. 6(c)] is positive and equal to ∼0.4 eV. The presence of gold on the surface prevents the oxidation of the NP, preventing the oxygen poisoning of the NP and allowing a better adsorption of CO [see Fig. 6(d)]. From another point of view this behavior will interfere with CO oxidation via both Langmuir-Hinshelwood and Eley-Rideal mechanisms, whereas Au@Cu nanoparticles are suitable for reactions according to these mechanisms. The adsorption of CO on the Au@Cu NPs [Fig. 6(d)] also does not depend on the local atomic environment and has a slightly negative value of the adsorption energy of about −0.25 eV.

For a more visual representation of the change in adsorption energy depending on the local atomic environment and composition, we have plotted the dependence of the average adsorption energy of O and CO on these properties as shown in Fig. 7. The difference between the adsorption energies of O and CO on the surfaces of pure Cu and Au nanoparticles
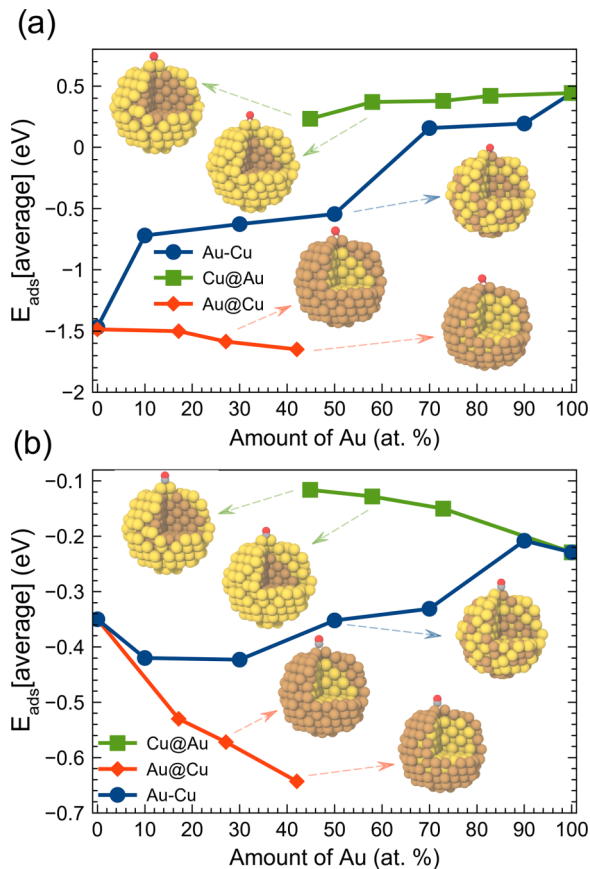
FIG. 7. Average adsorption energy of (a) O and (b) CO on AuCu NPs with different local atomic environment (Cu@Au, Au@Cu, and Au-Cu) as a function of composition. The gold and copper atoms are depicted as yellow and brown spheres, respectively.
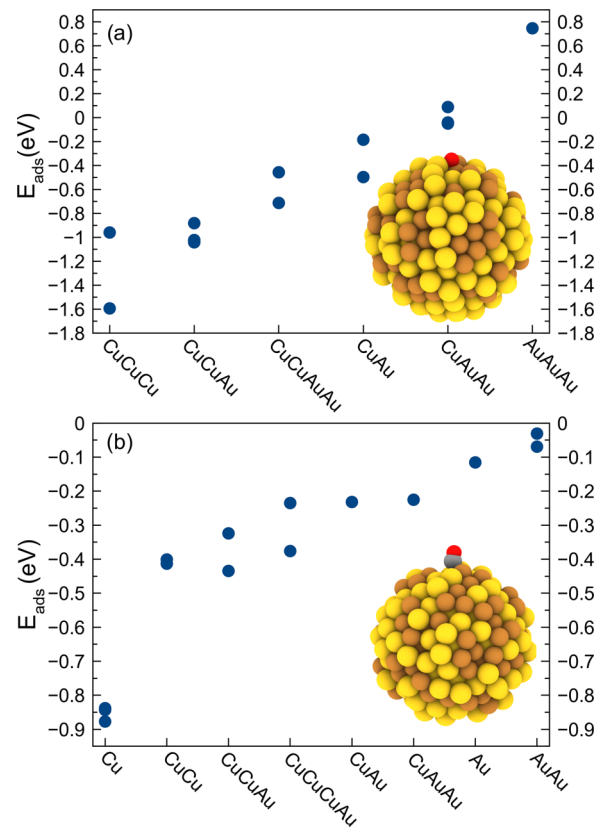

FIG. 8. Adsorption energies of (a) O atoms and (b) CO molecules on the considered bimetallic Cu-Au alloy (50% Cu, 50% Au) nanoparticle for various compositions and adsorption sites. The gold and copper atoms are depicted as yellow and brown spheres, respectively.

is 1.92 eV (-1.48 eV for Cu NP and 0.44 eV for Au NP). For Au@Cu particles, as the concentration of gold in the core increases and the thickness of the copper shell decreases, the adsorption energy decreases from -1.48 eV for pure Cu NP to -1.65 eV for Au@Cu with an atomic-thick Cu shell. In the case of Cu@Au NPs, a decrease in the number of Au atoms in the shell leads to a decrease in the adsorption energy of oxygen atoms from 0.44 eV for pure Au NP to 0.23 eV for Cu@Au with atomic-thick Au shell (the adsorption energy value is still positive). For the bimetallic alloy NP (50% Cu, 50% Au) the average adsorption energy of O atoms is -0.54 eV. However, in the case of the bimetallic alloy NP, the adsorption energy will strongly depend on the type of adsorption site (the variety of compositions is greater compared to pure metal surfaces). For example in Fig. 8(a) we have shown the dependence of the adsorption energy on the type of adsorption site. The site which consisting only of Cu atoms binds oxygen more strongly than mixed Cu-Au sites, whereas pure Au sites are not locally stable for the adsorption of these species.

In the case of the CO molecule, the change in the structure of the NP and its composition leads to more interesting trend [Fig. 7(b)]. The adsorption energy of the CO molecule is reduced by half compared to a Cu particle as the thickness of the Cu shell increases (for the same size and structure

type). The adsorption energies vary from -0.35 eV for pure Cu to -0.64 eV for $Au_{0.42}@Cu_{0.58}$. For bimetallic Au-Cu alloy particle (50% Cu, 50% Au) the change in adsorption energy of the CO molecule is not as large as for oxygen. At sites where there are more Cu atoms, CO molecules have the strongest binding [Fig. 8(b)]. This has been described in detail in our previous work [77]. A change in the structure type of the nanoparticles has a major effect on the binding energy of the CO molecule to the surface due to the change in the local atomic environment with subsequent change in the surface charge distribution (see Fig. 3). This is because CO prefers to bind to positively charged sites rather than negatively charged sites due to its more pronounced electron donating nature [80,81].

IV. CONCLUSIONS

Here we have studied the influence of composition (Cu:Au ratio), structure type (fcc, icosahedral, and amorphous), and local atomic environment (core-shell and alloy) of bimetallic AuCu nanoparticles with a diameter of 2 nm (321 atoms) on the electronic properties and charge distribution. It was found that the type of core-shell nanoparticles (Cu@Au and Au@Cu) together with the thickness of the shell with respect to the core drastically affects the surface charge. Nanoparticles in which the Cu core is covered by an atomic-thick Au shell

(Cu@Au) show a significant excess of electrons flowing from the copper core to the gold surface, forming a negative charge on the surface. Nanoparticles with an Au core covered by an atomic-thick Cu shell (Au@Cu) showed the opposite results, namely a deficiency of electrons on the surface forming a positive surface charge. At the same time, the structure type (fcc, icosahedral, and amorphous) of core-shell nanoparticles has almost no effect on the surface charge. For alloy nanoparticles, the surface charge is independent of changes in all properties (composition, local atomic environment, and structure type). The calculated d-band center for all considered nanoparticles shows their great potential for catalysis. The lower the value of the d-band center, the weaker the binding energy of the adsorbents with the metal surface. We observed the lowest value of the d-band center among the considered nanoparticles in Cu@Au core-shell nanostructures. The adsorption of O and CO on the surface of AuCu nanoparticles with fcc structure type has been studied in detail by considering 14 symmetrical nonequivalent adsorption sites. We show that the presence of Au on Cu@Au nanoparticles preserves the adsorption of O, which interferes with CO oxidation via both Langmuir-Hinshelwood and Eley-Rideal mechanisms, while Au@Cu nanoparticles are suitable for reactions according to these mechanisms. Alloy bimetallic fcc nanoparticles show a much broader distribution of adsorption energies for both O and CO adsorption. The obtained data correlate with the change in surface charge and d-band center in the case of adsorption of CO molecules, while in the case of O atoms the correlation is not so obvious. The results of this study open up great prospects for tuning the catalytic properties of nanocatalysts by modifying of their local atomic environment.

[1] S. Liu, Y. Li, X. Yu, S. Han, Y. Zhou, Y. Yang, H. Zhang, Z. Jiang, C. Zhu, W.-X. Li *et al.*, Tuning crystal-phase of bimetallic single-nanoparticle for catalytic hydrogenation, Nat. Commun. **13**, 4559 (2022).

[2] J. Liu, C. Lee, Y. Hu, Z. Liang, R. Ji, X. Y. D. Soo, Q. Zhu, and Q. Yan, Recent progress in intermetallic nanocrystals for electrocatalysis: From binary to ternary to high-entropy intermetallics, SmartMat **4**, e1210 (2023).

[3] K. Philippot and A. Roucoux, *Nanoparticles in Catalysis: Advances in Synthesis and Applications* (John Wiley & Sons, New York, 2021).

[4] A. S. Konopatsky, D. V. Leybo, K. L. Firestein, I. V. Chepkasov, Z. I. Popov, E. S. Permyakova, I. N. Volkov, A. M. Kovalskii, A. T. Matveev, D. V. Shtansky *et al.*, Polyol synthesis of Ag/Bn nanohybrids and their catalytic stability in CO oxidation reaction, ChemCatChem **12**, 1691 (2020).

[5] A. M. Kovalskii, I. N. Volkov, N. D. Evdokimenko, O. P. Tkachenko, D. V. Leybo, I. V. Chepkasov, Z. I. Popov, A. T. Matveev, A. Manakhov, E. S. Permyakova *et al.*, Hexagonal BN-and BNO-supported Au and Pt nanocatalysts in carbon monoxide oxidation and carbon dioxide hydrogenation reactions, Appl. Cataly. B: Environ. **303**, 120891 (2022).

[6] A. S. Konopatsky, K. L. Firestein, N. D. Evdokimenko, A. L. Kustov, V. S. Baidyshev, I. V. Chepkasov, Z. I. Popov, A. T. Matveev, I. V. Shetinin, D. V. Leybo *et al.*, Microstructure and catalytic properties of Fe$_3$O$_4$/Bn, Fe$_3$O$_4$ (Pt)/BN, and FePt/BN heterogeneous nanomaterials in CO$_2$ hydrogenation reaction: Experimental and theoretical insights, J. Catal. **402**, 130 (2021).

[7] D. Leybo, K. L. Firestein, N. D. Evdokimenko, A. A. Ryzhova, V. S. Baidyshev, I. V. Chepkasov, Z. I. Popov, A. L. Kustov, A. S. Konopatsky, D. V. Golberg *et al.*, Ball-milled processed, selective Fe/H-BN nanocatalysts for CO$_2$ hydrogenation, ACS Appl. Nano Mater. **5**, 16475 (2022).

[8] Z. Weng, Y. Wu, M. Wang, J. Jiang, K. Yang, S. Huo, X.-F. Wang, Q. Ma, G. W. Brudvig, V. S. Batista *et al.*, Active sites of copper-complex catalytic materials for electrochemical carbon dioxide reduction, Nat. Commun. **9**, 1 (2018).

[9] Z. Weng, J. Jiang, Y. Wu, Z. Wu, X. Guo, K. L. Materna, W. Liu, V. S. Batista, G. W. Brudvig, and H. Wang, Electrochemical CO$_2$ reduction to hydrocarbons on a heterogeneous molecular Cu catalyst in aqueous solution, J. Am. Chem. Soc. **138**, 8076 (2016).

[10] M. B. Gawande, A. Goswami, F.-X. Felpin, T. Asefa, X. Huang, R. Silva, X. Zou, R. Zboril, and R. S. Varma, Cu and Cu-based nanoparticles: Synthesis and applications in catalysis, Chem. Rev. **116**, 3722 (2016).

[11] A. S. K. Hashmi and G. J. Hutchings, Gold-katalyse, Angew. Chem. **118**, 8064 (2006).

[12] S. Kuang, M. Li, X. Chen, H. Chi, J. Lin, Z. Hu, S. Hu, S. Zhang, and X. Ma, Intermetallic CuAu nanoalloy for stable electrochemical CO$_2$ reduction, Chin. Chem. Lett. **34**, 108013 (2023).

[13] D. Kim, C. Xie, N. Becknell, Y. Yu, M. Karamad, K. Chan, E. J. Crumlin, J. K. Nørskov, and P. Yang, Electrochemical activation of CO$_2$ through atomic ordering transformations of aucu nanoparticles, J. Am. Chem. Soc. **139**, 8329 (2017).

[14] M. K. Birhanu, M.-C. Tsai, C.-T. Chen, A. W. Kahsay, T. S. Zeleke, K. B. Ibrahim, C.-J. Huang, Y.-F. Liao, W.-N. Su, and B. J. Hwang, Electrocatalytic reduction of carbon dioxide on gold–copper bimetallic nanoparticles: Effects of surface composition on selectivity, Electrochim. Acta **356**, 136756 (2020).

[15] Q. Gao, B. Yao, H. S. Pillai, W. Zang, X. Han, Y. Liu, S.-W. Yu, Z. Yan, B. Min, S. Zhang *et al.*, Publisher correction: Synthesis of core/shell nanocrystals with ordered intermetallic single-atom alloy layers for nitrate electroreduction to ammonia, Nat. Synth. **2**, 458 (2023).

[16] Y. Guan, Y. Liu, Q. Ren, Z. Dong, and L. Luo, Oxidation-induced phase separation of carbon-supported CuAu nanoparticles for electrochemical reduction of CO$_2$, Nano Res. **16**, 2119 (2023).

[17] Q. Sun, Y. Zhao, X. Tan, C. Jia, Z. Su, Q. Meyer, M. I. Ahmed, and C. Zhao, Atomically dispersed Cu–Au alloy for efficient electrocatalytic reduction of carbon monoxide to acetate, ACS Catal. **13**, 5689 (2023).

[18] A. A. Mikhailova, S. V. Lepeshkin, V. S. Baturin, A. P. Maltsev, Y. A. Uspenskii, and A. R. Oganov, Ultralow reaction barriers for CO oxidation in Cu–Au nanoclusters, Nanoscale **15**, 13699 (2023).

[19] X. Liu, A. Wang, L. Li, T. Zhang, C.-Y. Mou, and J.-F. Lee, Structural changes of Au–Cu bimetallic catalysts in CO oxidation: In situ XRD, EPR, XANES, and FT-IR characterizations, J. Catal. **278**, 288 (2011).

[20] S. Chen, S. V. Jenkins, J. Tao, Y. Zhu, and J. Chen, Anisotropic seeded growth of Cu–M (M= Au, Pt, or Pd) bimetallic nanorods with tunable optical and catalytic properties, J. Phys. Chem. C **117**, 8924 (2013).

[21] L. Ranno, S. D. Forno, and J. Lischner, Computational design of bimetallic core-shell nanoparticles for hot-carrier photocatalysis, npj Comput. Mater. **4**, 31 (2018).

[22] N. Eom, M. E. Messing, J. Johansson, and K. Deppert, General trends in core–shell preferences for bimetallic nanoparticles, ACS Nano **15**, 8883 (2021).

[23] Y. Wang, Q. Zhang, Y. Wang, L. V. Besteiro, Y. Liu, H. Tan, Z. M. Wang, A. O. Govorov, J. Z. Zhang, J. K. Cooper *et al.*, Ultrastable plasmonic Cu-based core–shell nanoparticles, Chem. Mater. **33**, 695 (2021).

[24] B. Corona, M. Howard, L. Zhang, and G. Henkelman, Computational screening of core@ shell nanoparticles for the hydrogen evolution and oxygen reduction reactions, J. Chem. Phys. **145**, 244708 (2016).

[25] J. Hao, B. Liu, S. Maenosono, and J. Yang, One-pot synthesis of Au-M@SiO$_2$ (M= Rh, Pd, Ir, Pt) core–shell nanoparticles as highly efficient catalysts for the reduction of 4-nitrophenol, Sci. Rep. **12**, 7615 (2022).

[26] X. Zhang, S. Han, B. Zhu, G. Zhang, X. Li, Y. Gao, Z. Wu, B. Yang, Y. Liu, W. Baaziz *et al.*, Reversible loss of core–shell structure for Ni–Au bimetallic nanoparticles during CO$_2$ hydrogenation, Nat. Catal. **3**, 411 (2020).

[27] Q. Guan, C. Zhu, Y. Lin, E. I. Vovk, X. Zhou, Y. Yang, H. Yu, L. Cao, H. Wang, X. Zhang *et al.*, Bimetallic monolayer catalyst breaks the activity–selectivity trade-off on metal particle size for efficient chemoselective hydrogenations, Nat. Catal. **4**, 840 (2021).

[28] R. Ferrando *et al.*, Growth pathways of exotic cu@ au core@shell structures: The key role of misfit strain, Nanoscale **15**, 1953 (2023).

[29] P. Strasser, S. Koh, T. Anniyev, J. Greeley, K. More, C. Yu, Z. Liu, S. Kaya, D. Nordlund, H. Ogasawara *et al.*, Lattice-strain control of the activity in dealloyed core–shell fuel cell catalysts, Nat. Chem. **2**, 454 (2010).

[30] J. E. van der Hoeven, J. Jelic, L. A. Olthof, G. Totarella, R. J. van Dijk-Moes, J.-M. Krafft, C. Louis, F. Studt, A. van Blaaderen, and P. E. de Jongh, Unlocking synergy in bimetallic catalysts by core–shell design, Nat. Mater. **20**, 1216 (2021).

[31] M. Luo and S. Guo, Strain-controlled electrocatalysis on multimetallic nanomaterials, Nat. Rev. Mater. **2**, 17059 (2017).

[32] X. Zhang, Z. Sun, R. Jin, C. Zhu, C. Zhao, Y. Lin, Q. Guan, L. Cao, H. Wang, S. Li *et al.*, Conjugated dual size effect of core-shell particles synergizes bimetallic catalysis, Nat. Commun. **14**, 530 (2023).

[33] B. Hammer and J. K. Nørskov, Theoretical surface science and catalysis-calculations and concepts, in *Advances in Catalysis*, Vol. 45 (Elsevier, Amsterdam, 2000), pp. 71–129.

[34] S. Zha, Z.-J. Zhao, S. Chen, S. Liu, T. Liu, F. Studt, and J. Gong, Predicting the catalytic activity of surface oxidation reactions by ionization energies, CCS Chem. **2**, 262 (2020).

[35] F. Calle-Vallejo, J. I. Martínez, J. M. García-Lastra, P. Sautet, and D. Loffreda, Fast prediction of adsorption properties for platinum nanocatalysts with generalized coordination numbers, Angew. Chem. Int. Ed. **53**, 8316 (2014).

[36] L. J. Sham and W. Kohn, One-particle properties of an inhomogeneous interacting electron gas, Phys. Rev. **145**, 561 (1966).

[37] P. Hohenberg and W. Kohn, Inhomogeneous electron gas, Phys. Rev. **136**, B864 (1964).

[38] B. Hammer, L. B. Hansen, and J. K. Nørskov, Improved adsorption energetics within density-functional theory using revised Perdew-Burke-Ernzerhof functionals, Phys. Rev. B **59**, 7413 (1999).

[39] G. Kresse and J. Hafner, Norm-conserving and ultrasoft pseudopotentials for first-row and transition elements, J. Phys.: Condens. Matter **6**, 8245 (1994).

[40] G. Kresse and J. Hafner, *Ab initio* molecular-dynamics simulation of the liquid-metal–amorphous-semiconductor transition in germanium, Phys. Rev. B **49**, 14251 (1994).

[41] G. Kresse and J. Furthmüller, Efficient iterative schemes for *ab initio* total-energy calculations using a plane-wave basis set, Phys. Rev. B **54**, 11169 (1996).

[42] P. E. Blöchl, Projector augmented-wave method, Phys. Rev. B **50**, 17953 (1994).

[43] S. Grimme, Semiempirical GGA-type density functional constructed with a long-range dispersion correction, J. Comput. Chem. **27**, 1787 (2006).

[44] S. Grimme, J. Antony, S. Ehrlich, and H. Krieg, A consistent and accurate *ab initio* parametrization of density functional dispersion correction (DFT-D) for the 94 elements H-Pu, J. Chem. Phys. **132**, 154104 (2010).

[45] S. Grimme, S. Ehrlich, and L. Goerigk, Effect of the damping function in dispersion corrected density functional theory, J. Comput. Chem. **32**, 1456 (2011).

[46] A. Tkatchenko, R. A. DiStasio Jr, R. Car, and M. Scheffler, Accurate and efficient method for many-body van der Waals interactions, Phys. Rev. Lett. **108**, 236402 (2012).

[47] A. Tkatchenko and M. Scheffler, Accurate molecular van der Waals interactions from ground-state electron density and free-atom reference data, Phys. Rev. Lett. **102**, 073005 (2009).

[48] S. N. Steinmann and C. Corminboeuf, A generalized-gradient approximation exchange hole model for dispersion coefficients, J. Chem. Phys. **134**, 044117 (2011).

[49] T. Gould, S. Lebegue, J. G. Ángyán, and T. Bučko, A fractionally ionic approach to polarizability and van der Waals many-body dispersion calculations, J. Chem. Theory Comput. **12**, 5920 (2016).

[50] M. Dion, H. Rydberg, E. Schröder, D. C. Langreth, and B. I. Lundqvist, Van der Waals density functional for general geometries, Phys. Rev. Lett. **92**, 246401 (2004).

[51] J. Klimeš, D. R. Bowler, and A. Michaelides, Van der Waals density functionals applied to solids, Phys. Rev. B **83**, 195131 (2011).

[52] J. B. Davis, F. Baletto, and R. L. Johnston, The effect of dispersion correction on the adsorption of CO on metallic nanoparticles, J. Phys. Chem. A **119**, 9703 (2015).

[53] T. Bučko, S. Lebegue, J. Hafner, and J. G. Angyan, Improved density dependent correction for the description of london dispersion forces, J. Chem. Theory Comput. **9**, 4293 (2013).

[54] J. Klimeš, D. R. Bowler, and A. Michaelides, Chemical accuracy for the van der Waals density functional, J. Phys.: Condens. Matter **22**, 022201 (2010).

[55] I. Hamada, van der Waals density functional made accurate, Phys. Rev. B **89**, 121103(R) (2014).

[56] H. Peng, Z.-H. Yang, J. P. Perdew, and J. Sun, Versatile van der Waals density functional based on a meta-generalized gradient approximation, Phys. Rev. X **6**, 041005 (2016).

[57] A. Stukowski, Visualization and analysis of atomistic simulation data with Ovito—The open visualization tool, Modell. Simul. Mater. Sci. Eng. **18**, 015012 (2010).

[58] K. Momma and F. Izumi, Vesta: A three-dimensional visualization system for electronic and structural analysis, J. Appl. Crystallogr. **41**, 653 (2008).

[59] K. Momma and F. Izumi, Vesta 3 for three-dimensional visualization of crystal, volumetric and morphology data, J. Appl. Crystallogr. **44**, 1272 (2011).

[60] W. Tang, E. Sanville, and G. Henkelman, A grid-based bader analysis algorithm without Lattice bias, J. Phys.: Condens. Matter **21**, 084204 (2009).

[61] R. Ferrando, G. Rossi, A. C. Levi, Z. Kuntová, F. Nita, A. Jelea, C. Mottet, G. Barcaro, A. Fortunelli, and J. Goniakowski, Structures of metal nanoparticles adsorbed on MgO(001). i. Ag and Au, J. Chem. Phys. **130**, 174702 (2009).

[62] Q. Wang, A. Nassereddine, D. Loffreda, C. Ricolleau, D. Alloyeau, C. Louis, L. Delannoy, J. Nelayah, and H. Guesmi, Cu segregation in Au–Cu nanoparticles exposed to hydrogen atmospheric pressure: How is fcc symmetry maintained? Faraday Discuss. **242**, 375 (2023).

[63] U. Pal, J. F. Sanchez Ramirez, H. Liu, A. Medina, and J. Ascencio, Synthesis and structure determination of bimetallic Au/Cu nanoparticles, Appl. Phys. A **79**, 79 (2004).

[64] Y. Y. Gafner, S. Gafner, and I. Chepkasov, The effect of thermal treatment on the organization of copper and nickel nanoclusters synthesized from the gas phase, J. Exp. Theor. Phys. **111**, 608 (2010).

[65] I. Chepkasov, Y. Y. Gafner, and S. Gafner, Changing of the shape and structure of cu nanoclusters generated from a gas phase: Md simulations, J. Aerosol Sci. **91**, 33 (2016).

[66] I. V. Chepkasov, Y. Y. Gafner, M. Vysotin, and L. Redel', A study of melting of various types of Pt–Pd nanoparticles, Phys. Solid State **59**, 2076 (2017).

[67] I. Chepkasov, Y. Y. Gafner, and S. Gafner, Synthesis of Cu nanoparticles by condensation from the gas phase, Phase Trans. **90**, 590 (2017).

[68] F. R. Boer, *Cohesion in Metals: Transition Metal Alloys*, Vol. 1 (North Holland, Amsterdam, 1988).

[69] W. Tyson and W. Miller, Surface free energies of solid metals: Estimation from liquid surface tension measurements, Surf. Sci. **62**, 267 (1977).

[70] H. Dong, C. Liu, Y. Li, and D.-E. Jiang, Computational screening of M/Cu core/shell nanoparticles and their applications for the electro-chemical reduction of CO_2 and CO, Nanoscale **11**, 11351 (2019).

[71] M. Dhifallah, M. Iachella, A. Dhouib, F. Di Renzo, D. Loffreda, and H. Guesmi, Support effects examined by a comparative theoretical study of Au, Cu, and CuAu nanoclusters on rutile and anatase surfaces, J. Phys. Chem. C **123**, 4892 (2019).

[72] I. Chepkasov, V. Baidyshev, and A. Baev, Structural properties of CuAu nanoparticles with different type. molecular dynamic simulations, J. Phys.: Conf. Ser. **1015**, 032022 (2018).

[73] P. Williams, Y. Mishin, and J. Hamilton, An embedded-atom potential for the Cu–Ag system, Modell. Simul. Mater. Sci. Eng. **14**, 817 (2006).

[74] I. Chepkasov, M. Visotin, E. Kovaleva, A. Manakhov, V. Baidyshev, and Z. Popov, Stability and electronic properties of PtPd nanoparticles via MD and DFT calculations, J. Phys. Chem. C **122**, 18070 (2018).

[75] A. Patra, J. E. Bates, J. Sun, and J. P. Perdew, Properties of real metallic surfaces: Effects of density functional semilocality and van der Waals nonlocality, Proc. Natl. Acad. Sci. USA **114**, E9188 (2017).

[76] S. Jiao, X. Fu, and H. Huang, Descriptors for the evaluation of electrocatalytic reactions: D-band theory and beyond, Adv. Funct. Mater. **32**, 2107651 (2022).

[77] I. V. Chepkasov, V. S. Baidyshev, A. A. Golubnichiy, I. S. Zamulin, A. G. Kvashnin, and S. M. Kozlov, Cu-Au nanoparticles produced by the aggregation of gas-phase metal atoms for co oxidation, Aggregate **3**, e273 (2022).

[78] X. Ma and H. Xin, Orbitalwise coordination number for predicting adsorption properties of metal nanocatalysts, Phys. Rev. Lett. **118**, 036101 (2017).

[79] See Supplemental Material at http://link.aps.org/supplemental/10.1103/PhysRevB.108.205414 for theadsorption energies of CO species calculated for 14 symmetric non-equivalent adsorption sites on fcc core-shell nanoparticles Cu@Au with fixed and unfixed metal atoms and illustrations of considered adsorption sites for O and CO.

[80] X.-N. Li, Z. Yuan, and S.-G. He, Co oxidation promoted by gold atoms supported on titanium oxide cluster anions, J. Am. Chem. Soc. **136**, 3617 (2014).

[81] J.-J. Chen, X.-N. Li, Q. Chen, Q.-Y. Liu, L.-X. Jiang, and S.-G. He, Neutral Au_1-Doped Cluster Catalysts $AuTi_2O_{3-6}$ for CO Oxidation by O_2, J. Am. Chem. Soc. **141**, 2027 (2019).